RSC Advances

ROYAL SOCIETY OF CHEMISTRY

www.rsc.org/advances

Cite this: DOI: 10.1039/c0xx00000x

www.rsc.org/xxxxxx

ARTICLE TYPE

3D ordered nanoporous $NiMoO_4$ for high-performance supercapacitor electrode materials

Seyyed Ebrahim Moosavifard,*[a] Javad Shamsi,[b] Saeed Fani,[c] Saeid Kadkhodazade[d]

Received (in XXX, XXX) Xth XXXXXXXXX 20XX, Accepted Xth XXXXXXXXX 20XX

DOI: 10.1039/b000000x

3D ordered nanocrystalline nanoporous $NiMoO_4$ has been synthesized by nanocasting from mesoporous silica KIT-6, and characterized by low and wide-angle powder X-ray diffraction (PXRD), high-resolution scanning electron microscopy (HR-SEM), transmission electron microscopy (TEM), BET, and BJH techniques, confirming formation of 3D high-ordered nanoporous structure of nanocrystalline (~ 9 nm) $NiMoO_4$ with high specific surface area (141 m^2 g^{-1}) and bimodal pore size distribution (4.5 and 12.5 nm). The electrochemical properties of the nanoporous $NiMoO_4$ have been evaluated as electrode material for supercapacitor in a three-electrode configuration in aqueous 3 M KOH solution. The material exhibits superior electrochemical performance including high area specific capacitance (ASC) of 4.25 F cm^{-2} (2835 F g^{-1}) at 3 mA cm^{-2}, excellent rate capability (2.18 F cm^{-2} at 120 mA cm^{-2}), excellent cycling stability in 6000 continuous cycles at different current densities (only 8.4% loss after 3000 cycles at 7.5 mA cm^{-2}), and high energy and power densities (141.75 Wh kg^{-1} in 0.6 kW kg^{-1},and 72.6 Wh kg^{-1} in 24 kW kg^{-1}). The superior electrochemical performance of the nanoporous $NiMoO_4$ electrode has been attributed to its structural features, including 3D high-ordered nanoporous structure with conjunct bimodal pores which facilitates mass transfer and electrolyte accessibility, high specific surface area which provides more active sites for the pseudocapacitive reactions, and nanosized walls which shorten diffusion paths. These results make the 3D nanoporous $NiMoO_4$ a promising electrode material for high-performance supercapacitors.

1. Introduction

In the 21st century, energy is one of the most important topics. With the increasing demand for energy and rapid depletion of fossil fuels and deteriorating environmental pollution, intense research has focused on renewable and clean energy sources with high capacitance and quicker charge-discharge rates in a small volume.[1, 2] Among some of the most practical systems such as lithium-ion batteries and fuel cells, supercapacitors (SCs) have attracted great attention as a promising candidate for energy storage due to their fast recharge ability, long cycle life, high power performance, and low maintenance cost.[3]

On the basis of energy storage mechanisms, SCs are classified into two main types: (a) electrical doublelayer capacitors (EDLCs), where capacitance arises from the charge separation at the electrode/electrolyte interface; (b) fast Faradaic redox reactions (psudocapacitance), where capacitance arises from reversible Faradaic reactions occurring at the electrode/electrolyte interface.[4-6] Generally, carbon materials with high specific surface area are used for EDLCs; conducting polymers and metal oxides are applied in pseudocapacitors.[6-8] Compared to EDLCs, pseudocapacitors provide times higher capacitance. Theoretically, EDLCs can bear a typical capacitance value of only 10-40 µF cm^{-2}, whereas pseudocapacitors can have capacitance values of 10-100 times that of EDLCs.[9-11] Specific capacitances of conductive polymers are lower than most of metal oxides and poor electrochemical stability of these materials need to be further improved.[12] Therefore, metal oxides have been considered to be the most promising materials for high-performance pseudocapacitors. Among metal oxides, binary metal oxide/hydroxides possessing multiple oxidation states that enable multiple redox reactions have been reported to exhibit a higher performance than single component oxides.[13, 14] Recently, metal molybdates, an important family of inorganic materials such as $CoMoO_4$,[15] $NiMoO_4$,[16] $MnMoO_4$,[17] have been extensively studied in various fields due to their low-cost, environmental friendliness and abundant resources.[18] Among them, $NiMoO_4$ possessing higher specific capacitance has been considered to be a promising candidate for the electrode materials for high-performance supercapacitors because of its enhanced electrochemical performance arising from high electrochemical activity of the nickel ions.[19] The electrochemical performance of these supercapacitors is determined primarily by the active sites for pseudocapacitive reactions, accessibility of electrolyte, short transport/diffusion paths and kinetics of its electrodes.[20, 21] Ordered nanoporous structures are good candidates owing to their high surface area, large pore volume, controllable narrow pore size and particle size.[22, 23] Among the various ordered nanoporous structures, the three-dimensional (3D) structures have attracted more attention because they have interconnected pores, larger

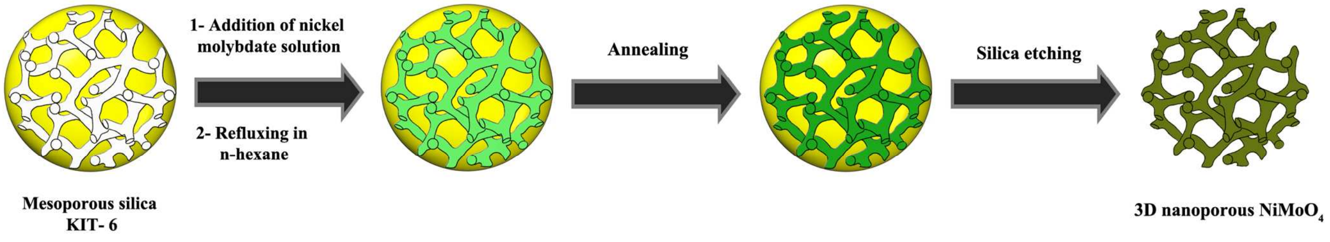

Scheme 1 Preparation of 3D ordered nanoporous $NiMoO_4$ by nanocasting from mesoporous silica KIT-6.

surface areas, lower wall thickness, better permeabilities and more active sites.[24-26] Until now, a few researches have reported $NiMoO_4$ as a supercapacitor electrode material. Herein, for the first time, we report a 3D ordered nanoporous $NiMoO_4$ with bimodal pore size distribution as a high performance supercapacitor electrode material. Remarkably, this 3D ordered nanoporous $NiMoO_4$ exhibits high specific capacitance and attractive rate capability with excellent cycling stability in various current densities, and demonstrates the importance and great potential of nanostructure metal molybdates in the development of high performance energy storage systems.

2. Experimental

2.1. Synthesis of 3D ordered nanoporous $NiMoO_4$

3D ordered nanoporous $NiMoO_4$ was synthesized by nanocasting from mesoporous silica KIT-6. For the first step, mesoporous silica KIT-6 template was synthesized according to previous reports.[27, 28] A typical synthesis procedure is as follows: 10 g of copolymer Pluronic P123 (average MW~5800, Aldrich) was mixed with 360 mL of doubly distilled water and 16 mL of concentrated HCl (37 wt %, Merck). The mixture was stirred at room temperature until a homogeneous solution was obtained. It was then transferred to an oil bath at 35 °C and 10 g of n-butanol (Merck) was added, and stirred for 1 h before the addition of 21.5 g of tetraethyl orthosilicate (TEOS, Merck). After stirring at 35 °C for 24 h, the mixture was transferred into an autoclave, which was sealed and maintained at 50 °C for another 24 h. After cooling down to room temperature, the precipitate was filtered, washed with an HCl/ethanol solution, and then large amount of distilled water. The final sample was dried at 60 °C overnight and calcined in air at 550 °C for 3 h to remove the polymer template. As shown in the scheme. 1, in a typical synthesis, 1.5 g of $Ni(NO_3)_2 \cdot 6H_2O$ (Merck) and 1.25 g of $Na_2MoO_4 \cdot 2H_2O$ (Merck) were dissolved in 10 mL ethanol to form a homogeneous solution. 1 g of mesoporous KIT-6 was dispersed in 50 mL of dried n-hexane (Merck) and stirred for 3 h at room temperature. Then, the nickel molybdate solution was added slowly with stirring. The mixture was then refluxed overnight, followed by filtering and drying at 60 °C until a completely dried powder was obtained. After that the sample was annealed at 400 °C for 3 hours. Then, to obtain nanoporous $NiMoO_4$, the resulting powder was treated twice with 4% HF solution to remove the silica template, followed by washing with distilled water and absolute ethanol several times, and then drying at 60 °C.

2.2. Synthesis of bulk $NiMoO_4$

$Ni(NO_3)_2 \cdot 6H_2O$ and $Na_2MoO_4 \cdot 2H_2O$ with molar ratio of 1 were dissolved in ethanol to form a homogeneous solution. Then, the solution was refluxed overnight in n-hexane, followed by filtering and drying at 60 °C until a completely dried powder was obtained. After that, the sample was annealed at 400 °C for 3 hours.

2.3. Characterization

Prepared sample was characterized using X-ray powder diffraction (XRD, Philips X'pert diffractometer with Cu Kα radiation (λ = 0.154 nm) generated at 40 kV and 30 mA with a step size of 0.04° s^{-1}). The morphology of the sample was investigated by an S-5500 high resolution scanning electron microscope (HR-SEM) from Hitachi and a JEOL JEM2010 (200 kV) transmission electron microscope (TEM). Nitrogen adsorption/desorption was determined at 77 K by Brunauer–Emmett–Teller (BET) measurements using an ASAP-2010 surface area analyzer. The pore size distribution was also obtained from desorption isotherm using Barrett-Joyner-Halenda (BJH) method.

2.4. Electrochemical measurements

For electrochemical measurements, the electrodes were prepared by mixing active material, acetylene black, and polyvinylidene fluoride (PVDF) with a mass ratio of 85:10:5. A 5% solution of the mixture in acetone was prepared and sprayed on nickel foam (as the current collector) and then dried in 120 °C for 2 h. The specific mass loading of the active material for the testing electrodes was about 1.5 mg cm^{-2}. The prepared electrode was used as the working electrode in a three-electrode configuration, while platinum plate and saturated calomel electrode (SCE) were used as the counter and reference electrodes, respectively. All potentials were referred to the reference electrode and all electrochemical measurements were performed at room temperature in aqueous 3 M KOH solution on a CHI 660D electrochemical workstation.

Specific capacitance of the electrodes was calculated through galvanostatic charge-discharge measurements using the following equation:

$$C_{sp} = \frac{I\Delta t}{m\Delta V} \quad (1)$$

where C_{sp} is the specific capacitance, I is the discharge current density in A, Δt is the discharge duration in s, m is the loaded mass of the active material in g, and ΔV is the potential range in V. Energy density was derived from the galvanostatic discharge curves using the following equation:

$$ED = \frac{C_{sp}\Delta V^2}{2} \quad (2)$$

where C_{sp} is specific capacitance in F g^{-1} and ΔV is the potential range in V. The power density of the electrode was calculated from the following equation:

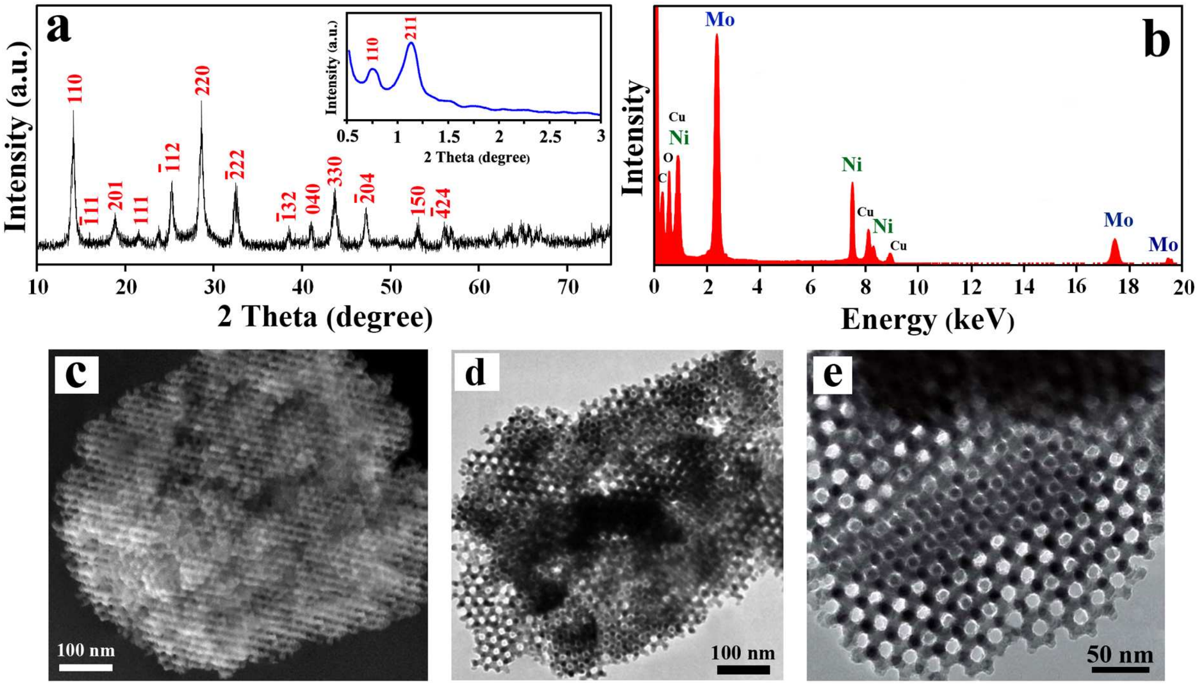

Fig 1. Wide-angle PXRD pattern of nanoporous $NiMoO_4$ .Inset is the low-angle PXRD (a), and the EDS spectrum of the nanoporous $NiMoO_4$ (b), and typical SEM image of the nanoporous $NiMoO_4$ (c), typical TEM images of the nanoporous $NiMoO_4$ at low magnification (d) and high magnification (e).

$$PD = \frac{ED}{\Delta t} \tag{3}$$

where ED is the energy density in Wh kg^{-1}, and Δt is the discharge time.

3. Results and discussion

3.1. Structural characterization

Detailed analyses for KIT-6 structure are given in the Supporting Information in Fig. S1†. The ordered mesostructures and crystalline nature of $NiMoO_4$ were confirmed by low- and wide-angle PXRD, respectively. Figs. 1a and S2a† show the wide-angle PXRD of the nanoporous and bulk $NiMoO_4$, respectively. As indicated, all of the diffraction peaks are well matched with the standard pattern of monoclinic $NiMoO_4$ (JCPDS card No. 86-0361). Moreover, the low base line in the patterns related to amorphous phases, indicates the almost complete removal of the silica template.[29] The inset of Fig. 1a shows the low-angle PXRD pattern of the ordered nanoporous $NiMoO_4$. The intense peak at 2θ of 1-1.2° corresponding to the (211) reflection, can be attributed to the presence of a 3D ordered mesostructure, and another weak peak at 2θ of 0.6-0.8° corresponds to the (110) diffraction peak.[30-32] The presence of weak (110) reflection indicates that the cubic (*I*a3d) mesostructure is slightly transformed to the tetragonal ($I4_132$) or lower mesostructure after removal of the silica template.[33-35]

The composition of the 3D ordered nanoporous $NiMoO_4$ was confirmed by energy dispersive X-ray spectroscopy (EDS) analysis under a N_2 atmosphere. As shown in Fig. 1b, the Ni, Mo, and O peaks are observed in this spectrum, suggesting that the sample is mainly composed of Ni, Mo, and O. The actual molar ratio of Ni and Mo obtained from EDX analysis is close to 1, which is near the stoichiometric composition and further confirms the formation of $NiMoO_4$. The Cu and C peaks come from the copper sample holder and preparation procedure of sample prior to examination by SEM, respectively. Furthermore, the lack of Si peak indicates the complete removal of the silica template.

The morphology and pore topology of the nanoporous $NiMoO_4$ were characterized by HR-SEM and TEM (Fig. 1c-e). As one can see from these images, the high-ordered 3D nanoporous structure is clearly visible over a long distance without the presence of bulk $NiMoO_4$. The open pores have a diameter around 13 nm, and the average crystallite size (wall thickness) was estimated to be around 9 nm which is slightly smaller than the value (11 nm) calculated by Scherrer equation from the XRD pattern. However, this small difference is not unusual, because the Scherrer equation gives volume averaged particle size while TEM analysis typically leads to a number average size.

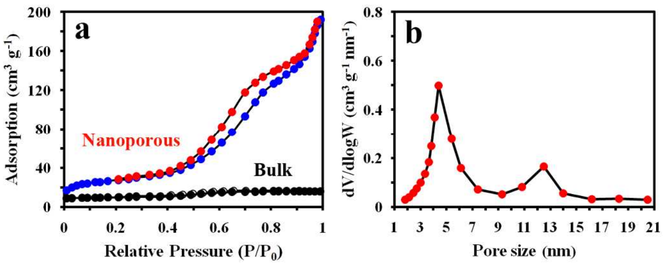

Fig. 2 Nitrogen adsorption-desorption isotherms of $NiMoO_4$ samples (a), and BJH desorption pore size distribution plot of nanoporous $NiMoO_4$ (b).

The porosity and textural parameters of $NiMoO_4$ samples were investigated by nitrogen physisorption. The nitrogen adsorption-desorption isotherms and the pore size distribution for high-ordered nanoporous and bulk $NiMoO_4$ are presented in Fig. 2. As

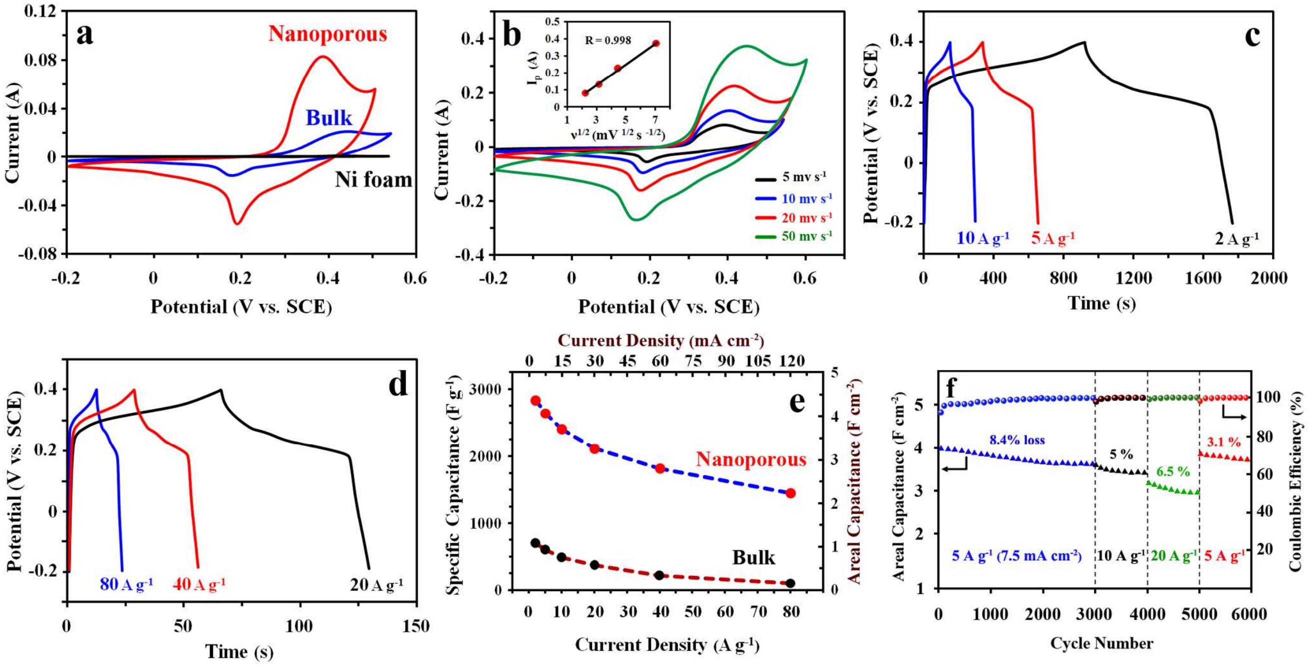

Fig. 3 CV of the bare Ni foam (current collector) and the as-prepared $NiMoO_4$ electrodes at a scan rate of 5 mV s^{-1} in aqueous 3 M KOH electrolyte (a), CV curves of the nanoporous $NiMoO_4$ electrode at various scan rates (inset is relationship between the anodic peak currents and square root of scan rate) (b), galvanostatic charge-discharge curves of the nanoporous $NiMoO_4$ electrode at various current densities (c, d), rate capability of the $NiMoO_4$ electrodes (e), cycling performance and coulombic efficiency of the nanoporous $NiMoO_4$ electrode at different current densities (f).

seen in Fig. 2a, the bulk sample has a type II isotherm that is characteristic for non-porous or macroporous materials, and the nanocast sample has a type IV isotherm that is characteristic for mesoporous or nanoporous materials.[36, 37] The nanoporous $NiMoO_4$ has a BET surface area of 141 m^2 g^{-1}, which is much higher than that of bulk $NiMoO_4$ (9.5 m^2 g^{-1}). Furthermore, as one can see from Fig. 2b, the nanoporous $NiMoO_4$ has a bimodal pore size distribution (calculated from desorption branch of the isotherm by the BJH method) centered at 4.5 and 12.5 nm. Smaller pores related to the wall thickness of the KIT-6 template indicate that in some regions the $NiMoO_4$ grows in both channels of KIT-6, while larger pores equal to the total value of the one of pore size and wall thickness of the KIT-6 template indicate that in some part the $NiMoO_4$ grows only in one channel of the template.[38, 39] This high-ordered nanoporous structure with conjunct bimodal pore size, nanocrystalline wall structure and high surface area can play key role in providing rapid electrolyte transport and shorter diffusion paths, while provides more active sites for electrochemical reactions.[4, 40, 41]

3.2. Electrochemical properties

To evaluate the electrochemical properties of the as-prepared samples, cyclic voltammetry (CV) and chronopotentiometry (CP) measurements were conducted in a three-electrode cell containing a 3 M KOH aqueous solution as the electrolyte. Fig. 3a shows the typical CVs of the bare electrode (Ni foam), bulk and nanoporous $NiMoO_4$ electrodes at a scan rate of 5 mV s^{-1}. As shown, the currents generated by the Ni foam are quite negligible as compared with those of the other two $NiMoO_4$ electrodes, revealing the almost no capacitance contribution of the current collector. Remarkably, the currents generated by the nanoporous $NiMoO_4$ electrode are much larger than those of the bulk $NiMoO_4$ electrode, indicating a significant increase of the areal capacitance. A pair of well-defined strong redox peaks clearly found from the CVs of the $NiMoO_4$ electrodes reveals the pseudocapacitive characteristics of the electrodes. These strong peaks are mainly attributed to the reversible redox Faradaic reaction of Ni(II)/Ni(III).[42, 43] The difference between the anodic and cathodic peak potentials is a readily measurable value in order to evaluate the reversibility of the redox reactions. The difference between the anodic (0.39 V) and cathodic (0.19 V) peak potentials for nanoporous $NiMoO_4$ electrode is lower than that of bulk $NiMoO_4$ (0.27 V). Lower ΔE_p suggests that nanoporous $NiMoO_4$ electrode has a higher reversibility, and can utilize more active material during charge-discharge process.[44, 45] Meanwhile, the current responses and voltammetric charges of the nanoporous $NiMoO_4$ electrode are much higher than those of bulk $NiMoO_4$, revealing much more charge storage. Fig. 3b shows the CV curves of the nanoporous $NiMoO_4$ electrode at various scan rates ranged from 5 to 50 mV s^{-1}. It is clearly seen that, with the increase of scan rate, the shape of the CV curves is not significantly influenced. This indicates the improved mass transportation, high rate capability and good reversibility of the material.[19, 46] Furthermore, with the increase of scan rate from 5 to 50 mV s^{-1}, the anodic peak potential slightly shifts from 0.39 to 0.45 V, indicating a relatively low internal resistance of the electrode.[47, 48] The linear relationship between the square root of the scan rate and the anodic peak currents (inset of Fig. 3b) reveals a diffusion controlled electrochemical reaction.

In order to evaluate the application of nanoporous $NiMoO_4$ as supercapacitor electrode materials, galvanostatic charge-discharge measurements were performed in the voltage range between -0.2 and 0.4 V at current densities between 3 and 120 mA cm^{-2} (2 and 80 A g^{-1}). As can be seen in Fig. 3c and 3d, the obvious nonlinear shape of the charge-discharge curves reveals that the capacitance of the nanoporous $NiMoO_4$ electrode is mainly originated from Faradaic reactions, which is in agreement with the result of the CV curves. The area specific capacitance (ASC) values for nanoporous $NiMoO_4$ electrode calculated from the charge-discharge tests are 4.25, 3.96, 3.61, 3.18, 2.73 and 2.18 F cm^{-2} (2835, 2642, 2408, 2117, 1820, and 1452 F g^{-1}, respectively) at current densities of 3, 7.5, 15, 30, 60, and 120 mA cm^{-2}, respectively. The ASC values for bulk $NiMoO_4$ electrode are 1.05, 0.9, 0.73, 0.56, 0.33 and 0.16 F cm^{-2} (701, 599, 487, 370, 217, and 108 F g^{-1}) at current densities of 3, 7.5, 15, 30, 60, and 120 mA cm^{-2}, respectively. The specific capacitance values of nanoporous $NiMoO_4$ electrode are substantially higher than those of bulk $NiMoO_4$ and the other reported psedocapacitive materials including $NiMoO_4$,[42, 46, 49-55] NiO,[56, 57] $Ni(OH)_2$,[58, 59] $NiCo_2O_4$,[14, 60] Co_3O_4.[61, 62] In order to give a better representation, the relationships between SC and ASC values and current densities for bulk and nanoporous $NiMoO_4$ electrodes are illustrated in Fig. 3e. As expected, the capacitance decreased with increasing current density due to the limited diffusion on the electrode surface, and insufficient active material involved in redox reaction at higher current densities. However, even at a high current density of 120 mA cm^{-2} (80 A g^{-1}), the nanoporous $NiMoO_4$ electrode shows a high capacitance of 2.18 F cm^{-2} (about 51% retention). This suggests an excellent rate capability for the nanoporous $NiMoO_4$ electrode under very high current density operation condition which is significant in practical supercapacitor applications. Moreover, this high ASC at the large current density (2.18 F cm^{-2} at 120 mA cm^{-2}) reported here is higher than those reported $NiMoO_4$ materials, such as $NiMoO_4$ nanowires (1.96 F cm^{-2} at 112 mA cm^{-2}),[43] $NiMoO_4$ nanosheets (1.51 F cm^{-2} at 30 mA cm^{-2}) and $NiMoO_4$ nanowires (1.91 F cm^{-2} at 30 mA cm^{-2}),[22] even higher than $NiCo_2O_4$@MnO_2 core-shell heterostructured nanowire arrays (1.66 F cm^{-2} at 20 mA cm^{-2}).[63]

The long-term cycling stability of the nanoporous $NiMoO_4$ electrode was also investigated by continuous charge-discharge measurements over 6000 cycles at different current densities as shown in Fig. 3f. As can be seen, at the current density of 5 A g^{-1} (7.5 mA cm^{-2}), the ASC gradually decreases to 3.63 F cm^{-2} (2420 F g^{-1}) after 3000 cycles corresponding to a capacitance loss of 8.4%. In the next 1000 cycles (at 10 A g^{-1} or 15 mA cm^{-2}) the ASC decreased to 95% of its initial value, and after the next 1000 cycles (at 20 A g^{-1} or 30 mA cm^{-2}), the sample retained about 93.5% of its capacitance. After 5000 continuous cycles at successively increased current densities, the capacitance recovered to 3.87 F cm^{-2} (2580 F g^{-1}) when the current density was turned back to 5 A g^{-1}. The next 1000 cycles exhibited excellent stability with about 96.9% capacitance retention. These observations demonstrate excellent cycling performance of nanoporous $NiMoO_4$ at different current densities. Furthermore, as can be seen in Fig. 3f, the columbic efficiency of the sample during 6000 continuous cycles indicates excellent reversibility of the material during charge-discharge. The long-term cycling stability of the bulk $NiMoO_4$ electrode was also investigated over 3000 cycles (ESI, Fig. S3†) at the current density of 5 A g^{-1} (7.5 mA cm^{-2}). Different from that of the nanoporous $NiMoO_4$ electrode, the capacitance of the bulk $NiMoO_4$ electrode decreases sharply during the first 1500 cycles, and then it keeps nearly steady from the 1500th to 3000th cycle. After 3000 cycles, the specific capacitance retained about 42% of its initial value, which is much lower than that of nanoporous $NiMoO_4$ electrode.

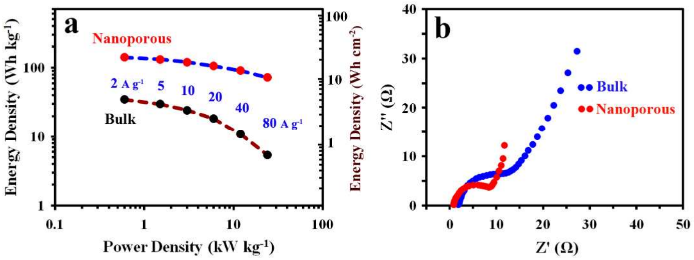

Fig. 4 Ragone plot for $NiMoO_4$ electrodes at different current densities (a), EIS plot of the $NiMoO_4$ electrodes at open circuit potential.

Energy density (ED) and power density (PD) of a supercapacitor, determining its operational performance/efficiency, are considered the most important parameters in supercapacitor devices.[64] As shown in Fig. 4a, in order to demonstrate the overall performance of the $NiMoO_4$ electrodes, the Ragone plot (PD vs. ED) is shown at various current densities. The superior energy density of 141.75 Wh kg^{-1} (21.3 × 10^{-5} Wh cm^{-2}) was achieved by the nanoporous $NiMoO_4$ at a power density of 0.6 kW kg^{-1}, while an energy density of 72.6 Wh kg^{-1} (10.9 × 10^{-5} Wh cm^{-2}) was observed at a high power density of 24 kW kg^{-1}, which is much higher than that of bulk sample and other previous reported $NiMoO_4$ electrodes.[49-55] In order to further characterization of the electrochemical behaviour of the $NiMoO_4$ electrodes, electrochemical impedance spectroscopy (EIS) was performed at open circuit potential and the Nyquist plots are shown in Fig. 4b. Depressed semicircle at the high frequency region, corresponded to the charge transfer resistance (R_{ct}),[65] was attributed to the redox reactions of the Ni(II)/Ni(III) redox couples. The straight line at the low frequency region, corresponded to the Warburg impedance (Z_w),[66] was related to the diffusion of electrolyte along the nanostructures. Obviously, the nanoporous $NiMoO_4$ electrode exhibits a lower charge transfer resistance (R_{ct}) and lower internal resistance (R_b), suggesting the larger electro-active surface area, and higher electrical conductivity of the electrode.[22] The nanoporous $NiMoO_4$ electrode also has a more ideal vertical line, which demonstrates that the nanoporous structure of the $NiMoO_4$ has reduced the mass-transfer resistance and enhanced the ion diffusion of electrolyte.[67] All these results demonstrate the excellent pseudo-capacitance characteristics feature of the nanoporous $NiMoO_4$ as a high-performance supercapacitor electrode material.

The superior electrochemical performance of the nanoporous $NiMoO_4$ could be attributed to the following structural features. First, the 3D high-ordered nanoporous structure with conjunct bimodal pores enhances the accessibility of electrolyte, and facilitates mass transfer in open and interconnected pores;[21, 23, 40] second, the high specific surface area provides more active sites for the pseudocapacitive reaction, and improves the utilization of the active material;[19, 68, 69] third, the nanosized walls provide a short transport/diffusion path for both ions and electrons, leading to faster kinetics and higher conductivity.[70-73] These results make the 3D nanoporous $NiMoO_4$ a promising electrode material for high-performance supercapacitors.

Conclusions

3D high-ordered nanocrystalline nanoporous $NiMoO_4$ with high surface area and bimodal pore size distribution was successfully synthesized by nanocasting from mesoporous silica KIT-6, and applied as supercapacitor electrode material. The nanoporous $NiMoO_4$ electrode exhibited superior electrochemical performance including high area specific capacitance (4.25 F cm^{-2} at 3 mA cm^{-2}), excellent rate capability, high energy density and excellent cycling stability at different current densities. This superior electrochemical performance was related to the structural features including 3D high-ordered nanoporous structure with conjunct bimodal pores, high specific surface area, and nanosized walls.

Notes and references

[a]*Young Researchers and Elite Club, Central Tehran Branch, Islamic Azad University, Tehran, Iran. Email: info_seyyed@yahoo.com; Tel/Fax: +98 21 82883455.*
[b]*Department of Chemistry, University of Tehran, Tehran, Iran.*
[c]*Department of Chemistry, University of Science and Technology, Tehran, Iran.*
[d]*Chemistry and Chemical Engineering Research Center of Iran, Tehran, Iran.*

† Electronic Supplementary Information (ESI) available: See DOI: 10.1039/b000000x/

1. M. Winter and R. J. Brodd, *Chem. Rev.*, 2004, **104**, 4245.
2. H. Wang, H. S. Casalongue, Y. Liang and H. Dai, *J. Am. Chem. Soc.*, 2010, **132**, 7472.
3. J. R. Miller and P. Simon, *Science*, 2008, **321**, 651.
4. P. Simon and Y. Gogotsi, *Nat. Mater.*, 2008, **7**, 845.
5. G. Wang, L. Zhang and J. Zhang, *Chem. Soc. Rev.*, 2012, **41**, 797.
6. Y. He, W. Chen, C. Gao, J. Zhou, X. Li and E. Xie, *Nanoscale*, 2013, **5**, 8799.
7. M. Zhi, C. Xiang, J. Li, M. Li and N. Wu, *Nanoscale*, 2013, **5**, 72.
8. X. Xia, Y. Zhang, D. Chao, C. Guan, Y. Zhang, L. Li, X. Ge, I. M. Bacho, J. Tu and H. J. Fan, *Nanoscale*, 2014, **6**, 5008.
9. B. E. Conway, *Electrochemical supercapacitors : scientific fundamentals and technological applications*, Plenum Press, New York, 1999.
10. S. K. Meher and G. R. Rao, *J. Phys. Chem. C*, 2011, **115**, 25543.
11. S. Liu, S. Sun and X. Z. You, *Nanoscale*, 2014, **6**, 2037.
12. D. Hulicova-Jurcakova, M. Kodama, S. Shiraishi, H. Hatori, Z. H. Zhu and G. Q. Lu, *Adv. Funct. Mater.*, 2009, **19**, 1800.
13. Z. Wu, Y. Zhu and X. Ji, *J. Mater. Chem. A*, 2014, **2**, 14759.
14. Z. Wang, Y. Zhang, Y. Li and H. Fu, *RSC Adv.*, 2014, **4**, 20234.
15. X. Yu, B. Lu and Z. Xu, *Adv. Mater.*, 2014, **26**, 1044.
16. X. Tang, L. Xiao, C. Yang, J. Lu and L. Zhuang, *Int. J. Hydrogen Energ.*, 2014, **39**, 3055.
17. D. Ghosh, S. Giri, M. Moniruzzaman, T. Basu, M. Mandal and C. K. Das, *Dalton Trans.*, 2014, **43**, 11067.
18. W. Xiao, J. S. Chen, C. M. Li, R. Xu and X. W. Lou, *Chem. Mater.*, 2009, **22**, 746.
19. M. C. Liu, L. B. Kong, C. Lu, X. J. Ma, X. M. Li, Y. C. Luo and L. Kang, *J. Mater. Chem. A*, 2013, **1**, 1380.
20. M. J. Deng, C. C. Wang, P. J. Ho, C. M. Lin, J. M. Chen and K. T. Lu, *J. Mater. Chem. A*, 2014, **2**, 12857.
21. Q. Lu, Y. Chen, W. Li, J. Chen, J. Q. Xiao and F. Jiao, *J. Mater. Chem. A*, 2013, **1**, 2331.
22. D. Cai, B. Liu, D. Wang, Y. Liu, L. Wang, H. Li, Y. Wang, C. Wang, Q. Li and T. Wang, *Electrochim. Acta*, 2014, **125**, 294.
23. G. Wang, H. Liu, J. Horvat, B. Wang, S. Qiao, J. Park and H. Ahn, *Chem. –Eur. J.*, 2010, **16**, 11020.
24. D. Liu, Z. Yang, P. Wang, F. Li, D. Wang and D. He, *Nanoscale*, 2013, **5**, 1917.
25. X. J. Ma, L. B. Kong, W. B. Zhang, M. C. Liu, Y. C. Luo and L. Kang, *Electrochim. Acta*, 2014, **130**, 660.
26. K. Xu, R. Zou, W. Li, Q. Liu, X. Liu, L. An and J. Hu, *J. Mater. Chem. A*, 2014, **2**, 10090.
27. T. W. Kim, F. Kleitz, B. Paul and R. Ryoo, *J. Am. Chem. Soc.*, 2005, **127**, 7601.
28. F. Jiao, A. H. Hill, A. Harrison, A. Berko, A. V. Chadwick and P. G. Bruce, *J. Am. Chem. Soc.*, 2008, **130**, 5262.
29. A. Aranda, B. Puértolas, B. Solsona, S. Agouram, R. Murillo, A. Mastral, S. Taylor and T. Garcia, *Catal. Lett.*, 2010, **134**, 110.
30. L. A. Solovyov, V. I. Zaikovskii, A. N. Shmakov, O. V. Belousov and R. Ryoo, *J. Phys. Chem. B*, 2002, **106**, 12198.
31. A. Rumplecker, F. Kleitz, E. L. Salabas and F. Schüth, *Chem. Mater.*, 2007, **19**, 485.
32. S. Sun, Z. Wen, J. Jin, Y. Cui and Y. Lu, *Microporous Mesoporous Mater.*, 2013, **169**, 242.
33. J. K. Shon, S. S. Kong, J. M. Kim, C. H. Ko, M. Jin, Y. Y. Lee, S. H. Hwang, J. A. Yoon and J. N. Kim, *Chem. Commun.*, 2009, **0**, 650.
34. Y. Doi, A. Takai, Y. Sakamoto, O. Terasaki, Y. Yamauchi and K. Kuroda, *Chem. Commun.*, 2010, **46**, 6365.
35. L. A. Solovyov, *Chem. Soc. Rev.*, 2013, **42**, 3708.
36. K. S. W. Sing, D. H. Everett, R. A. W. Haul, L. Moscou, R. A. Pierotti, J. Rouquerol and T. Siemieniewska, *Pure Appl. Chem.*, 1985, **57**, 603.
37. M. Anbia. S. E. Moosavi Fard, *Sensor. Actuat. B-Chem.*, 2011, **160**, 215.
38. H. Tüysüz, C. Weidenthaler, T. Grewe, E. L. Salabaş, M. J. Benitez Romero and F. Schüth, *Inorg. Chem.*, 2012, **51**, 11745.
39. T. Grewe, X. Deng, C. Weidenthaler, F. Schüth and H. Tüysüz, *Chem. Mater.*, 2013, **25**, 4926.
40. A. Walcarius, *Chem. Soc. Rev.*, 2013, **42**, 4098.
41. Y. Ye, C. Jo, I. Jeong and J. Lee, *Nanoscale*, 2013, **5**, 4584.
42. D. Cai, B. Liu, D. Wang, Y. Liu, L. Wang, H. Li, Y. Wang, C. Wang, Q. Li and T. Wang, *Electrochim. Acta*, 2014, **115**, 358.
43. D. Guo, P. Zhang, H. Zhang, X. Yu, J. Zhu, Q. Li and T. Wang, *J. Mater. Chem. A*, 2013, **1**, 9024.
44. J. Xu, Y. Dong, J. Cao, B. Guo, W. Wang and Z. Chen, *Electrochim. Acta*, 2013, **114**, 76.
45. C. C. Hu, J. C. Chen and K. H. Chang, *J. Power Sources*, 2013, **221**, 128.

46. B. Senthilkumar, K. Vijaya Sankar, R. Kalai Selvan, M. Danielle and M. Manickam, *RSC Adv.*, 2013, **3**, 352.
47. J. Yan, Z. Fan, W. Sun, G. Ning, T. Wei, Q. Zhang, R. Zhang, L. Zhi and F. Wei, *Adv. Funct. Mater.*, 2012, **22**, 2632.
48. G. Zhang and X. W. Lou, *Adv. Mater.*, 2013, **25**, 976.
49. D. Cai, D. Wang, B. Liu, Y. Wang, Y. Liu, L. Wang, H. Li, H. Huang, Q. Li and T. Wang, *ACS Appl. Mater. Interfaces*, 2013, **5**, 12905.
50. D. Ghosh, S. Giri and C. K. Das, *Nanoscale*, 2013, **5**, 10428.
51. M. C. Liu, L. Kang, L. B. Kong, C. Lu, X. J. Ma, X. M. Li and Y. C. Luo, *RSC Adv.*, 2013, **3**, 6472.
52. B. Senthilkumar, D. Meyrick, Y.-S. Lee and R. K. Selvan, *RSC Adv.*, 2013, **3**, 16542.
53. H. Wan, J. Jiang, X. Ji, L. Miao, L. Zhang, K. Xu, H. Chen and Y. Ruan, *Mater. Lett.*, 2013, **108**, 164.
54. B. Senthilkumar and R. Kalai Selvan, *J. Colloid Interf. Sci.*, 2014, **426**, 280.
55. D. Cai, D. Wang, B. Liu, L. Wang, Y. Liu, H. Li, Y. Wang, Q. Li and T. Wang, *ACS Appl. Mater. Interfaces*, 2014, **6**, 5050.
56. K. Liang, X. Tang and W. Hu, *J. Mater. Chem.*, 2012, **22**, 11062.
57. Y. Bai, M. Du, J. Chang, J. Sun and L. Gao, *J. Mater. Chem. A*, 2014, **2**, 3834.
58. H. W. Park, Y. T. Ju, S. M. Park and K. C. Roh, *RSC Adv.*, 2014, **4**, 567.
59. X. Ma, J. Liu, C. Liang, X. Gong and R. Che, *J. Mater. Chem. A*, 2014, **2**, 12692.
60. G. Zhang and X. W. Lou, *Sci. Rep.*, 2013, **3**.
61. C. Yuan, L. Zhang, L. Hou, G. Pang and W. C. Oh, *RSC Adv.*, 2014, **4**, 14408.
62. H. Wang, L. Zhang, X. Tan, C. M. B. Holt, B. Zahiri, B. C. Olsen and D. Mitlin, *J. Phys. Chem. C*, 2011, **115**, 17599.
63. L. Yu, G. Zhang, C. Yuan and X. W. Lou, *Chem. Commun.*, 2013, **49**, 137.
64. M. F. El-Kady, V. Strong, S. Dubin and R. B. Kaner, *Science*, 2012, **335**, 1326.
65. N. Li, J. Y. Wang, Z.Q. Liu, Y.P. Guo, D.Y. Wang, Y.Z. Su and S. Chen, *RSC Adv.*, 2014, **4**, 17274.
66. K. K. Purushothaman, B. Saravanakumar, I. M. Babu, B. Sethuraman and G. Muralidharan, *RSC Adv.*, 2014, **4**, 23485.
67. C. Guan, J. Liu, C. Cheng, H. Li, X. Li, W. Zhou, H. Zhang and H. J. Fan, *Energy Environ. Sci.*, 2011, **4**, 4496.
68. K. Pinkert, L. Giebeler, M. Herklotz, S. Oswald, J. Thomas, A. Meier, L. Borchardt, S. Kaskel, H. Ehrenberg and J. Eckert, *J. Mater. Chem. A*, 2013. **1**, 4904.
69. F. Bao, X. Wang, X. Zhao, Y. Wang, Y. Ji, H. Zhang and X. Liu, *RSC Adv.*, 2014, **4**, 2393.
70. C. Yuan, J. Li, L. Hou, X. Zhang, L. Shen and X. W. Lou, *Adv. Funct. Mater.*, 2012, **22**, 4592.
71. C. Yuan, L. Yang, L. Hou, L. Shen, X. Zhang and X. W. Lou, *Energy Environ. Sci.*, 2012, **5**, 7883.
72. T. Brezesinski, J. Wang, S. H. Tolbert and B. Dunn, *Nat. Mater.*, 2010, **9**, 146.
73. S. E. Moosavifard, J. Shamsi, S. Fani and S. Kadkhodazade, *Ceram. Int.*, 2014, **40**, 15973.